Journal of Hazardous Materials 403 (2021) 123921

Contents lists available at ScienceDirect

Journal of Hazardous Materials

journal homepage: www.elsevier.com/locate/jhazmat

Preparation and properties of a dual-function cellulose nanofiber-based bionic biosensor for detecting silver ions and acetylcholinesterase

Lei Wang [a,b], Wei Guo [a,b], Hongxiang Zhu [a,b], Hui He [a,b,*], Shuangfei Wang [a,b]

[a] College of Light Industry and Food Engineering, Guangxi University, Nanning, 530004, PR China
[b] Guangxi Key Laboratory of Clean Pulp & Papermaking and Pollution Control, Nanning, 530004, PR China

ARTICLE INFO

Editor: C. LingXin

Keywords:
CNF
DNA
Silver ions
AChE
Bionic

ABSTRACT

A dual-function cellulose nanofiber (CNF)-based bionic biosensor with good biocompatibility was developed for detecting Ag^+ and acetylcholinesterase (AChE) by grafting deoxyribonucleic acid (DNA) onto CNF. The Ag^+ ions captured by the biosensor acted as recognition sites for the detection of AChE. The CNF-based bionic biosensor (CNF-DNA) could detect Ag^+ concentrations as low as 10^{-6} nM in the presence of interference metal ions (Hg^{2+}, Ba^{2+}, Cd^{2+}, Mg^{2+}, Mn^{2+}, Pb^{2+}, and Zn^{2+}). DNA-template silver nanoclusters (DNA-AgNCs) were formed on the surface of CNF-DNA during the detection of Ag^+ (CNF-DNA-AgNCs). This new strategy yielded CNF-DNA-AgNCs through the adsorption of Ag^+ ions onto the cytosine base of the single-stranded DNA in CNF-DNA without the use of any additional reducer. Meanwhile, the CNF-DNA-AgNCs exhibited excellent sensitivity and selectivity for trace levels (0.053 mU/mL) of AChE in the presence of interference reagents. The novel strategy proposed in this paper may establish a foundation for further research on DNA-template AgNCs for developing biosensors and biomarkers for *in vivo* and *in vitro* detection.

1. Introduction

With the prosperous development of industry, the heavy metals are broadly used in various fields. Among the heavy metals ions, Ag^+ is the most common form of silver, and as a bioactive cation, it exhibits high antimicrobial activity even at trace concentrations (Spacciapoli et al., 2001). Ag^+ is widely used in photographic, electrical, and pharmaceutical industries (Goh et al., 2017). However, once the safe concentration is exceeded, Ag^+ will affect human health adversely (Li et al., 2017). Ag^+ is harmful for various fishes and microbes when the concentration was above 1.6 nmol/L. In addition, excessive Ag^+ causes to break the nutrient chain that leads to ecosystems destruction (Goh et al., 2017), and accumulates in the body inactivates sulfhydryl enzymes by interacting with sulfur atoms of many metabolites (Li et al., 2017). Therefore, the development of sensors with high sensitivity and selectivity for low-level detection of Ag^+ ions is important (Liu et al., 2019a). Thus, various Ag^+ ion sensors based on organic molecules (Ahmed et al., 2019; Desai et al., 2019), polymers (Liu et al., 2019b), nanoparticles (Wang et al., 2019; He et al., 2017; Wang et al., 2018), oligonucleotides (Guo et al., 2017; Zhang and Wei, 2017), DNA zymes (Liu et al., 2016; Xu et al., 2019a), and proteins (Khoris et al., 2019) have been developed. Oligonucleotide-based biosensors have gained immense attention over the past few years. These sensors interact strongly with bases instead of general univalent (sodium ion, potassium ion) and bivalent (magnesium ions, calcium ion) ions, which interact with the nucleotide phosphate back, and form stable mismatched base pairs (Wolfe et al., 2019). In 2008, Ono et al. (2008) reported that Ag^+ ions can interact with the cytosine base (C) to form a stable C-Ag^+-C mismatched complex. Since then, the C-Ag^+-C complex has gained significant attention for the detection of silver ions. The combination of acid (DNA) and the C-Ag^+-C complex has been used to develop various colorimetric biosensors (Xu et al., 2019b), fluorescent biosensors (Long et al., 2017; Zuo et al., 2016; Movahedi et al., 2019), electrochemical sensors (Pargar et al., 2018; Sun et al., 2019), force spectroscopy sensors (Choi et al., 2016; Jiang et al., 2019), and force microscopy sensors (Ko et al., 2017) for the sensitive detection of Ag^+ ions in water. However, DNA-based sensors exhibit low sensitivity and toxicity, and hence are not suitable for *in vivo* and *in vitro* detection in biomedical applications. Therefore, it is necessary to choose a matrix with good biocompatibility to prepare biosensors for *in vivo* and *in vitro* detection. Meanwhile, the multi-functionality of the C-Ag^+-C structure, which is formed during the detection of Ag^+ by DNA-based sensors, should be further improved.

* Corresponding author at: College of Light Industry and Food Engineering, Guangxi University, Nanning, 530004, PR China.
E-mail address: gxuhh@gxu.edu.cn (H. He).

https://doi.org/10.1016/j.jhazmat.2020.123921
Received 24 June 2020; Received in revised form 27 August 2020; Accepted 8 September 2020
Available online 13 September 2020

At present, fluorescent silver nanoclusters (AgNCs) have paid increasing attention because their significant impressive optical properties, facile synthesis method, low-cost, and excellence biocompatibility (Wang et al., 2020). Reducers are vital for the synthesis of AgNCs. In the absence of a reducer, AgNCs show irreversible aggregation, which reduces their surface area and deteriorates their fluorescence properties. Various reducers such as anionic polymers, peptides, and single-stranded DNA-template have been used for the synthesis of AgNCs (DNA-AgNCs). The synthesis of fluorescent DNA-AgNCs with single-stranded DNA as the template has gained extensive attention owing to their excellent optical properties, low toxicity, and excellent light stability and biocompatibility. Moreover, DNA-AgNCs emit AgNCs upon irradiation with visible-near-infrared light by changing the conformation of the DNA template. This makes DNA-AgNCs suitable for *in vitro* and *in vivo* detection in biomedical applications (Zhao et al., 2019). It has been reported that Ag^+ can interfere with the ionization regulation and neuromodulation processes in aquatic environments as well as the activity of plasma cholinesterase (ChE) in affected zebrafish after three days of exposure (Katuli et al., 2014). Acetylcholinesterase (AChE) is an important nervine enzyme involved in neural impulse transfer. In addition, AChE can accelerate the hydrolysis of acetylcholine (ACh), which is a central neurotransmitter, to acetic acid and choline (Liu et al., 2019c). The hydrolysis of Ach in the nervine system by AChE facilitates the assemblage of starch-like β proteins into starch-like fibrils, which is a procedure that leads to the Alzheimer's disease (AD) that AD is the reason of dementia and the fastest deteriorating neurodegenerative disease, which happened in the old persons. As well known, the amyloid hypothesis, that is to say, cerebral deposition of the amyloid-β peptide is the key pathological hallmark of AD and is relevant to the neuronal toxicity and synaptic disruption that displays in pathogenesis period (Kosmidis et al., 2018; Han et al., 2019). Recently, the suppression of neuroregulatory function resulting in an increase in the ACh content has been demonstrated to be a potential method for treating AD. Thus, the detection of AChE is highly important for curing AD.

Therefore, in this study, we prepared a novel nanosized CNF-based biosensor (CNF-DNA) with good biocompatibility, excellent selectivity, and high sensitivity for the detection of Ag^+ by grafting DNA onto the surface of CNFs. Interestingly, DNA-AgNCs were formed during the detection of Ag^+ by the CNF-DNA sensor (CNF-DNA-AgNCs). These CNF-DNA-AgNCs acted as recognition sites for detecting AChE. The strategy used in this study did not require any reducer to prepare the fluorescent CNF-DNA-AgNCs. Ag^+ adsorbed onto the cytosine of the single-stranded DNA of CNF-DNA and then reduced to AgNCs. Furthermore, the carboxyl groups on the surface of the CNF suppressed the aggregation of the DNA-AgNCs. Meanwhile, the DNA grafted onto the CNF endowed the CNF-DNA sensor with peeling resistance and high-signal intensity. Thus, the method proposed in this study can overcome the limitation of unstable and low signals of DNA biosensors prepared by physical methods. The physical and chemical structures and the Ag^+ and AChE sensitivity of the CNF-DNA sensor were investigated. The selective recognition mechanisms of the sensor for the detection of Ag^+ and AChE were also investigated.

2. Materials and methods

2.1. Materials and reagents

Bagasse pulp cellulose fibers(flexible, green, light-weight, and green.) were purchased from Guangxi Guangye Sugar Industry Group Co. Ltd. (Guigang, China). Acetylcholine chloride, bovine serum, methionine, homocysteine thiolactone hydrochloride, gamma-glutamyl transferase (γ-GT), glutamic pyruvic transaminase (GPT), and DNA (5′-NH_2-$(CH_2)_6$-CCCTTAATCCCC-3′) were provided by Kangwei company (Nanning, China). Sodium periodate, (2,2,6,6-Tetramethylpiperidin-1-yl)oxyl (TEMPO), sodium hypochlorite solution, sodium chlorite, sodium dihydrophosphate, dipotassium phosphate, 1-ethyl-3-(3-(dimethylamino) propyl) carbodiimide (EDC),N-hydroxysulfosuccinimide (NHS), AChE (from *Electrophorus electricus*), and a range of metal salts of analytical grade were obtained from Sigma-Aldrich. The other reagents were of analytical grade. All the solutions were prepared using ultrapure water (18.2 MΩ cm) obtained using a Milli-Q system.

2.2. Chemical structure and morphology characterization

Fourier-transform infrared spectroscopy (FT-IR) (SpectrumGX, USA), elemental analysis (EA) (Vario MACRO cube, Germany), transmission electron microscopy (TEM) (TF20 Joel2100 F), scanning electron microscopy (SEM) (Hitachi S4800, Japan), atomic force microscopy (AFM)(NT-MDT Prima), X-ray photoelectron spectroscopy (XPS) (Thermo-VG Scientific ESCALAB 250, USA), and solid ^{13}C nuclear magnetic resonance spectroscopy (NMR) (crown, Germany) were employed to investigate the physicochemical properties of the samples. The thermal stability of the samples was evaluated by carrying out their thermogravimetric analysis (TGA) (NETZSCH STA499F5, Germany) by heating them from 30 to 600 °C at a heating rate of 5 °C/min. The ultraviolet-visible (UV–vis) and fluorescence spectra of the samples were recorded on a UV–vis spectrometer (UV-1800, Japan) and fluorescence spectrometer (Cary Eclipse, Germany), respectively. A confocal laser scanning microscope (CLSM) (TCS SP8 X, Germany) was used to evaluate the biocompatibility of CNF-DNA.

2.3. Preparation of the CNF-DNA

Preparation of dialdehyde cellulose fibers (DACFs): Firstly, dry bagasse pulp cellulose fibers (CFs): 4.00 g and ultra-pure water (200.0 mL) were mixed in a three-necked flask (500 mL), and sodium periodate was put in the obtained dispersion liquid by 0.30 mol/L of a desired concentration. Then the flask was closely covered *via* the aluminum foil and mixed at 45 °C for 4 h. Lastly, ethylene glycol (15.6 mL) was added in the above mixture for ending the reaction. The final product was washed through ultra-pure water several times and then dried to a constant weight at 60 °C for 12 h. By measuring, the aldehyde groups content of the DACFs was 5.95 mmol/g.

Preparation of TEMPO oxidized DACFs (CNF): Firstly, DACFs (2.00 *g*) and phosphate buffer solution (180.0 mL, pH = 7.4) were mixed in a beaker and the obtained solution was churned by a rate of 500 rpm. Nextly, making TEMPO (0.04 *g*), hypochlorite solution (20.0 mL, 0.1 mol/L), and sodium chlorite (2.15 *g*) to add in the above mixture and then oxidized at 60 °C for 16 h. Lastly, ethanol (7.0 mL) was put in the obtained solution for stopping the reaction. The result was homogenized in a homogenizer 4 times until a solid-state content was fitted 1.5 %. The resulting solid was washed with ultra-pure water, segregated by centrifugation and freeze dried (36 h) to finally possess CNF. The carboxyl group content of the CNF was 1.502 mmol/g which measured by the method of acid-base titration. In addition, the FTIR spectra of the CFs, DACFs, and CNF were displayed (Fig. S1).

DNA could be grafted onto the surface of the CNF because of the presence of a large number of carboxyl groups (—COOH) on them (Fig. 1). First, NHS (0.01 g) and EDC (0.01 g) were added to 100 μL of a 1.5 wt% CNF solution under stirring at 25 °C for 1 h. To this solution, 10 OD of an amino-modified DNA was added to above solution (100 μL) while stirring at 25 °C for 24 h in order to graft the DNA aptamer onto the surface of the CNF. Subsequently, the unreacted excess DNA aptamers (molecular weight: 3680 Da), NHS (molecular weight: 115.09 Da), and EDC (molecular weight: 191.70 Da) were removed from the solution using a dialysis membrane filter (molecular weight cut-off: 50 kDa) until solution was neutral and store in refrigerator at 4 °C. The grafting degree (G, %) of CNF-DNA was calculated by Eq. (1).

$$G = \frac{(w \times m_2)/0.34}{m_1} \times 100\% \quad (1)$$

where w is the mass percentage of nitrogen element in the CNF-DNA, m_1 and m_2 is the weight of CNF and CNF-DNA, respectively, and 0.34

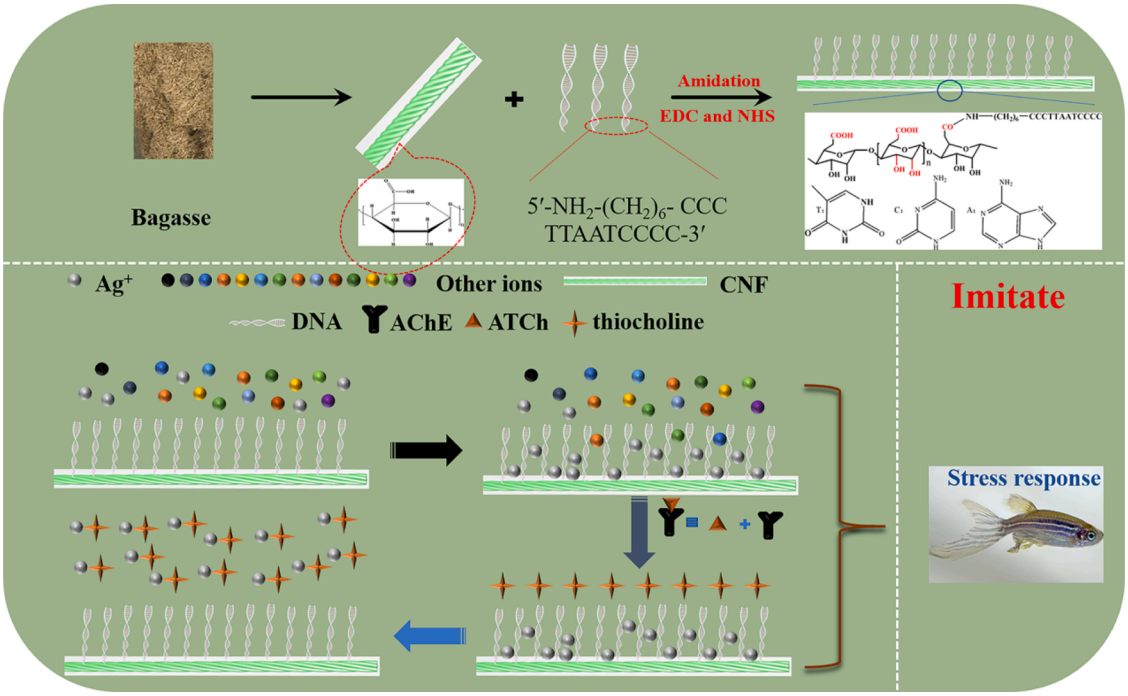

Fig. 1. Fabrication of CNF-DNA *via* chemical grafting and the selective recognition of Ag^+ ions and AChE.

represent content percentage of nitrogen element in the DNA. The grafting degree (G, %) of CNF-DNA based on CNF was 25.66 %.

2.4. Detection of Ag^+ by CNF-DNA

CNF-DNA (100 μL) was first blended with Ag^+ ions (100 μL; different concentrations). The resulting solution was stirred for 1 h and was then subjected to fluorescence spectroscopy measurements (given wavelength: 240 nm; solvent: ultra-pure water). The Ag^+ selectivity of CNF-DNA was investigated by adding interference metal ions (at a concentration of 1 nM) to the solution. The sensitivity of CNF-DNA towards Ag^+ was evaluated by adding Ag^+ ions to the solution at various concentrations (0, 20, 80, 100, 140, 160, and 200 nM). All the experiments were carried out at 25 °C.

2.5. Detection of AChE activity by CNF-DNA

For AChE activity detection, CNF-DNA (100 μL) was mixed with Ag^+ (200 nM) to prepare CNF-DNA-AgNCs. Then, the phosphate buffer (40 mM, pH 7.4), ATCh (10 μM), AChE (various activities), and the CNF-DNA-AgNCs (0.15 mg/mL) were blended, and the blend was reacted at 40 °C for 30 min. The fluorescence curve of the blend was obtained.

3. Results and discussion

3.1. Chemical characterization and morphology

The FTIR spectra of the CNF and CNF-DNA are shown in Fig. S2(a). The CNF showed four FTIR peaks at 3342 (—O—H stretching vibration) (Kruer-Zerhusen et al., 2017), 2897 (—C—H) (Rieger et al., 2016), 1103 (—C—O—C cytoskeleton vibration), and 897 (β-glycosidic bond) cm^{-1}. CNF-DNA showed three additional peaks at 1740 (H—N—C═O) (Zhou et al., 2020), 1460 (NH δ ip) (Mansour et al., 2017), and 1240 cm^{-1} (C-Nst) (Minnes et al., 2017), suggesting that the end amino of the DNA sequence was anchored onto the surface of the CNF. The chemical structures of the CNF and CNF-DNA were investigated by obtaining their solid-state ^{13}C NMR (Fig. S2**(b)**) spectra. The CNF showed chemical shifts at 60.55 (C-6), 62.75–76.43 (C-2, 3, 5), 84.25 and 79.83 (C-4), 100.42 (C-1) (Tian et al., 2017), and 170.6 ppm (—COOH). In the case of CNF-DNA the chemical shifts were observed at 170 (NH_2—C═O), 50.83 (C-7–C-13), 38.60 (C-15), 32.26 (C-16), 21.20 (C-17), and 10.82 ppm (C-14) (Ganapathy et al., 1981), suggesting that the carboxyl groups of the CNF were bonded with the end-amino of DNA *via* an amidation reaction.

The superficial (10 nm) element binding energies of the CNF and CNF-DNA were analyzed by XPS. The XPS curves (Fig. 2**(a)**) showed that N was not present on the surface of the CNF. On the other hand, CNF-DNA showed N 1s XPS peaks. The CNF showed four C 1s peaks at 288.42, 288.00, 286.53, and 284.85 eV corresponding to the C═O, β-glycosidic, C—O—H/C—O—C, and C—H/C—C groups, respectively (Fig. 2**(b)**) (Al-Enizi et al., 2018). In addition, the CNF showed two O 1s peaks at 532.76 and 531.64 eV corresponding to C—O—H/C—O—C and —COOH, respectively (Fig. 2**(c)**) (Zhu et al., 2017). CNF-DNA showed C1s peaks at 287.79, 286.46, 286.11, 285.48, 284.78, and 284.22 eV corresponding to the C═O, β-glycosidic, C—O—H/C—O—C, C═C, C—H/C—C, and C—N/C═N bonds, respectively (Fig. 2**(d)**) (Camacho et al., 2017). Furthermore, CNF-DNA showed O 1s peaks at 531.85 and 530.94 eV corresponding to the C—O—H/C—O—C and C═O/—COOH bonds, respectively (Fig. 2**(e)**) (Cho et al., 2011). The N 1s spectrum of CNF-DNA (Fig. 2**(f)**) showed three peaks at 401.26, 399.65, and 398.88 eV corresponding to C═N, O═C—N, and C—NH_2/C—NH, respectively (He et al., 2020). These results indicate that DNA was successfully grafted onto the surface of the CNF. CNF-DNA consisted of 7.12 wt% N, as revealed by the EA results, Table S1). These results indicate that a large amount of DNA was grafted onto the surface of the CNF. Fig. S4 shows the SEM, TEM, and AFM images of the CNF and CNF-DNA. The SEM and TEM images (Figs. S4**(a)**–**(d)**) revealed that the CNF and CNF-DNA were almost fibrous. Figs. **S4(e)** and **(f)** show the AFM images of the CNF and CNF-DNA, respectively. As, can be observed from the figures, the CNF surface became smoother after the grafting of DNA onto it. In addition, CNF-DNA showed good thermal stability (Fig. S5).

3.2. Selectivity and sensitivity of the CNF-DNA towards Ag^+

To investigate whether the CNF matrix enhanced the fluorescence and absorbance of CNF-DNA, a phosphate-buffered-saline solution (pH

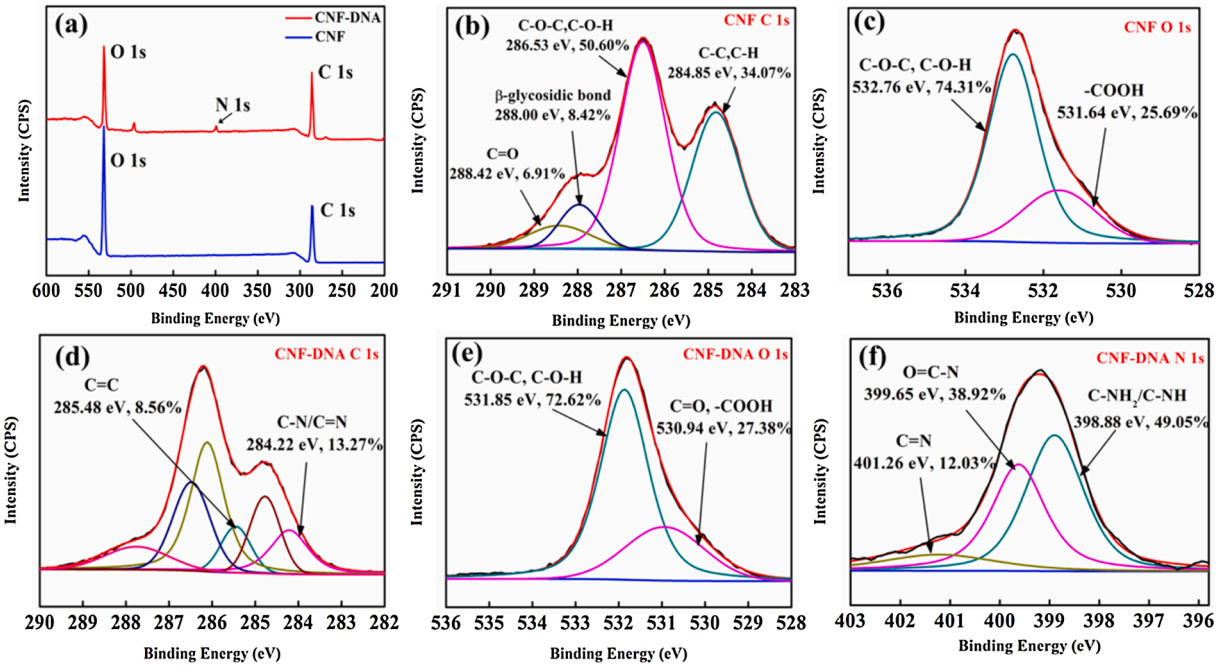

Fig. 2. XPS survey spectra of the CNFs and CNF-DNA (a); C 1s (b) and O 1s (c) spectra of the CNFs; C 1s (d), O 1s (e), and N 1p spectra (f) of CNF-DNA.

= 7.4) was mixed with DNA (10 OD), and $AgNO_3$ (200 nM) was added to the resulting solution. In the absence of the CNF, DNA showed low-intensity UV–vis and fluorescence signals (Fig. 3**(a)** and **(b)**). However, the absorbance and fluorescence peak intensities of CNF-DNA were about two times higher than those of DNA. This is reason that CNF of CNF-DNA can provide a solid platform with enhancing absorbance-ability. This indicates that the CNF matrix enhanced the absorbance and fluorescence of CNF-DNA. In addition, the physical mixture of CNF and DNA (CNF/DNA) showed no absorbance and fluorescence signals in the presence of 1 nM Ag^+. The reason may be attributed to the interaction between CNF and DNA by physical method was lower than chemical method, resulting in Ag^+ more stable rich on the surface of CNF-DNA than CNF/DNA, further improving intensity of the sensor. This suggests that it was necessary to graft DNA onto the surface of the CNF in order to achieve absorbance and fluorescence in the presence of Ag^+ ions. CNF exhibited high porosity, and the diffusion path lengths of the Ag^+ ions moving towards the CNF were short (Xing et al., 2015). Thus, the Ag^+ ions were immediately deposited on the surface of CNF-DNA and enhanced its absorbance and fluorescence.

In order to investigate the Ag^+ sensitivity of CNF-DNA, various Ag^+ concentrations were used. As shown in Fig. 3**(c)** and **(d)**, the intensities of the absorbance and fluorescence signals increased with an increase in the Ag^+ concentration from 0 to 200 nM. In order to quantitatively analyze the Ag^+ sensitivity of CNF-DNA, its absorbance and fluorescence intensities at 206 and 781 nm, respectively, as functions of the Ag^+ concentration were plotted. The absorbance intensities of CNF-DNA at the Ag^+ concentrations of 0–20 nM (Fig. 3**(e)**) were plotted and a linear plot with the equation y = 0.00393x+0.23414 (R^2 = 0.9969) was obtained. The fluorescence intensity of CNF-DNA showed a linear relationship with the Ag^+ concentration (0–80 nM) (Fig. 3**(f)**), y = 1.25369x-10.48824 (R^2 = 0.9970). The UV–vis and fluorescence spectral limits of detection (3 standard error/slope) (Rivilla et al., 2020) for

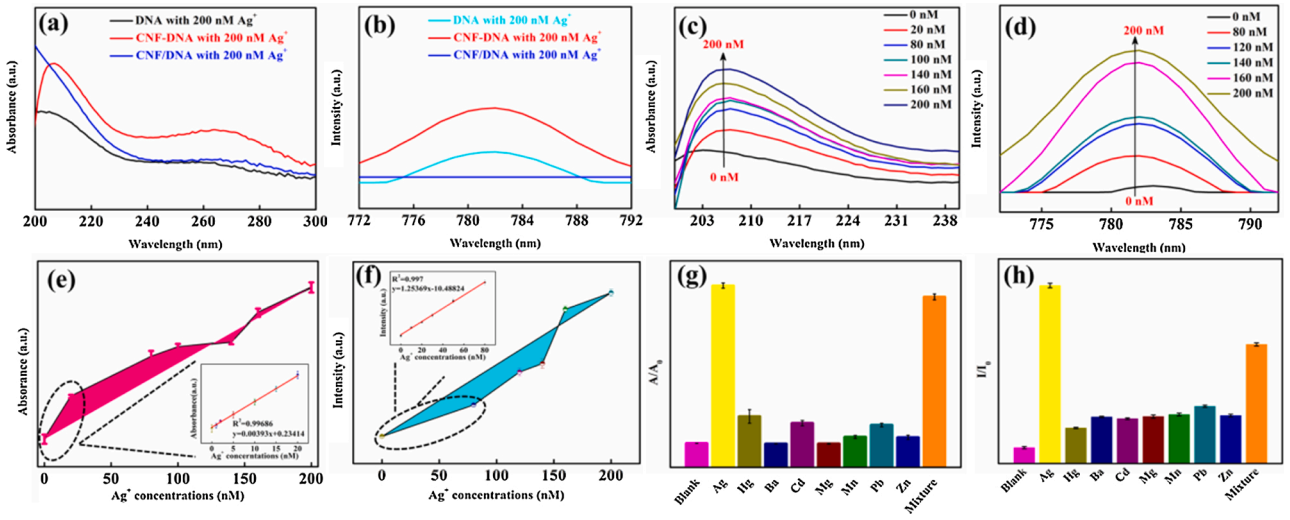

Fig. 3. UV vis (a) and fluorescence (b) spectra of DNA, CNF-DNA, and CNF/DNA (CNF mixed with DNA) with 200 nM Ag^+; UV–vis (c) and fluorescence spectra (d) of CNF-DNA with various Ag^+ concentrations; the corresponding calibration curves (e, f) obtained in the presence of Ag^+ at various concentrations; the linear relationship between the UV absorbance, fluorescent light intensity, and Ag^+ concentration (inset of c, d).

Ag^+ were as low as ~0.07 and 1×10^{-6} nM, respectively. These values are lower than the limits of detection reported previously for Ag^+ (Table S2). Thus, the CNF-DNA biosensor showed high sensitivity for trace amounts of Ag^+.

3.3. Formation of the CNF-DNA-AgNCs

The selectivity of CNF-DNA for Ag^+ detection in the presence of interference metal ions (Hg^{2+}, Ba^{2+}, Cd^{2+}, Mg^{2+}, Mn^{2+}, Pb^{2+}, H_2O, and Zn^{2+}) was investigated (Fig. 4). No significant increase was observed in the absorbance and fluorescence of CNF-DNA in the presence of the interference metal ions (Fig. 4**(a)** and **(b)**, respectively). These results indicated that only Ag^+ could effectively enhance the fluorescence intensity of CNF-DA. It has been reported (Long et al., 2017) that Ag^+ can interact with cytosine bases (C) to form stable C-Ag^+-C mismatch complexes and induce conformational changes of single-stranded DNA to emit fluorescence. Meanwhile, the DNA sequence (5′-NH_2-$(CH_2)_6$ -CCCTTAATCCCC-3′) have seven C sites which can quickly recognize Ag^+ and produce fluorescence enhancement effect. Therefore, CNF-DNA showed superior responsiveness to Ag^+. Moreover, owing to the cations of these solutions are dissolved from the corresponding sulfate, acetate, nitrate, or chloride, the related anions are bound to mix in the liquor. Thus, CNF-DNA also has the ability to resist the influence of anions with sulfate, acetate, nitrate, or chloride ions (Guo et al., 2019). Thus, the CNF-DNA biosensor showed outstanding selectivity for Ag^+.

It was found that DNA-AgNCs were formed on the surface of CNF-DNA during the detection of Ag^+. The effect of the Ag^+ concentration on the formation of the DNA-AgNCs was investigated (Fig. 5). The average size of the DNA-AgNCs formed on the surface of CNF-DNA increased with an increase in the Ag^+ concentration (Figs. S6, S7). The highest number of DNA-AgNCs was formed on the surface of CNF-DNA at the Ag^+ concentration of 1 nM (Fig. 5). The average size (2.13 nm, see Fig. S6**(a)**) of these nanoclusters (NCs) was smaller than the NCs obtained at all the other Ag^+ concentrations. Therefore, the Ag^+ concentration of 1 nM was found to be optimum for the formation of DNA-AgNCs on the surface of CNF-DNA. The CNF-DNA-AgNCs formed on the surface of CNF-DNA acted as recognition sites to detect AChE.

3.4. Selectivity and sensitivity of the CNF-DNA-AgNCs towards AChE

As can be observed from Fig. 6**(a)** and **(d)**, the absorbance and fluorescence peak intensities of the CNF-DNA-AgNCs increased with a decrease in the AChE activity from 0 to 50 mU/mL. To quantitatively investigate the sensitivity of the CNF-DNA-AgNCs towards the activity of AChE, their absorbance and fluorescence intensities at 204 and 723 nm, respectively, were plotted as functions of the AChE concentration. The absorbance intensities of the CNF-DNA-AgNCs at the AChE concentrations of 0–50 nM (Fig. 6**(b)**) were plotted and a linear plot with the equation y = 0.42582-0.00115x (R^2 = 0.991) was obtained. The fluorescence intensities of the CNF-DNA-AgNCs at the AChE concentrations of 0–45 nM (Fig. 6**(e)**) were plotted and a linear plot with the equation y = 0.09287–5.30216x (R^2 = 0.99847) was obtained. The UV–vis and fluorescence spectral limits of detection (3 standard error/slope) (Wang et al., 2020) for AChE were as low as ~0.108 and 0.053 mU/mL, respectively, which are smaller than those reported previously (Table S3). In addition, the selectivity of the CNF-DNA-AgNCs for the detection of AChE was investigated by adding other S-containing reagents (bovine serum, homocysteine, methionine, GPT, and γ-GT) to the solution, as shown in Fig. 6**(c)**. The absorbance and fluorescence of the CNF-DNA-AgNCs showed no significant decrease in the presence of the other interference reagents (Fig. 6**(f)**). Thus, the CNF-DNA-AgNCs showed excellent sensitivity and selectivity for AChE activity.

3.5. Recognition mechanism of CNF-DNA for the detection of Ag^+ and AChE

To investigate the Ag^+ detection mechanism of CNF-DNA, the XPS survey spectra of CNF-DNA and the CNF-DNA-AgNCs were obtained (Fig. 7**(a)**). The CNF-DNA-AgNCs showed Ag 3d peaks (366.08–382.08 eV). (Fig. 7**(b)**). The Ag 3d peak of the CNF-DNA-AgNCs could be deconvoluted into a $3d_{5/2}$ peak at 368.68 eV and a $3d_{3/2}$ peak at 374.78 eV (Gao et al., 2016). This confirms that Ag^+ could be detected by CNF-DNA. This Ag^+ then chelated with CNF-DNA to form the CNF-DNA-AgNCs.

The N 1s peak of the CNF-DNA-AgNCs (Fig. 7**(c)**) could be deconvoluted into three peaks at 398.11 (24.39 %), 399.16 (48.54 %), and 400.00 (27.07 %) eV, corresponding to N—Ag, C═N, and C—NH_2/C—NH, respectively (Volkov et al., 2017). These results Journal indicate that the amino group (—NH_2) in DNA chelated with Ag^+. Besides, the CNF-DNA-AgNCs showed O 1s curves (Fig. 7**(d)**) at 530.1 (26.42 %), 531.43 (48.12 %), and 535.14 (25.46 %) eV corresponding to —COOH/C═O, C—O—H/C—O—C, and O—Ag (Zhu et al., 2019), respectively. This indicates that O atoms played a vital role in the interaction between CNF-DNA and Ag^+. In addition, the size of the CNF-DNA average nanoparticles was found to be 2.13 nm. The sizes of the nanoparticles and AgNCs (1–10 nm) (Burratti et al., 2019) obtained were consistent with those obtained from the TEM (Fig. 5b) results. This indicates that some of the Ag^+ from the solution was captured by CNF-DNA and reduced to form NCs. Comparing with N 1s curves and O 1s curves in Fig. 2, the —NH_2 peak and the —COOH peak of CNF-DNA-AgNCs was smaller by XPS. That also confiem Ag^+ was reduced to form NCs. Ag^+ exhibited fluorescence while being captured

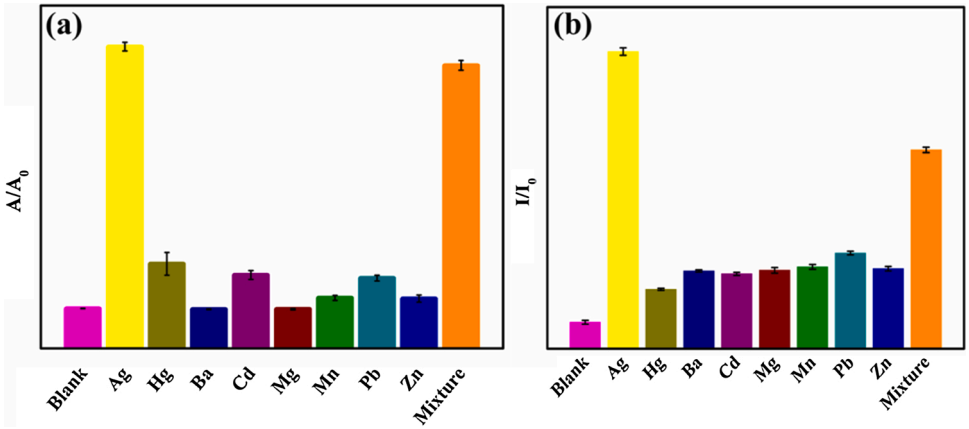

Fig. 4. UV–vis and fluorescence responses of CNF-DNA towards 1 nM Ag^+, with 1 nM interference metal ions. (Mixture was the mixed metal ions solution, including Ag^+, Hg^{2+}, Ba^{2+}, Cd^{2+}, Mg^{2+}, Mn^{2+}, Pb^{2+}, and Zn^{2+}).

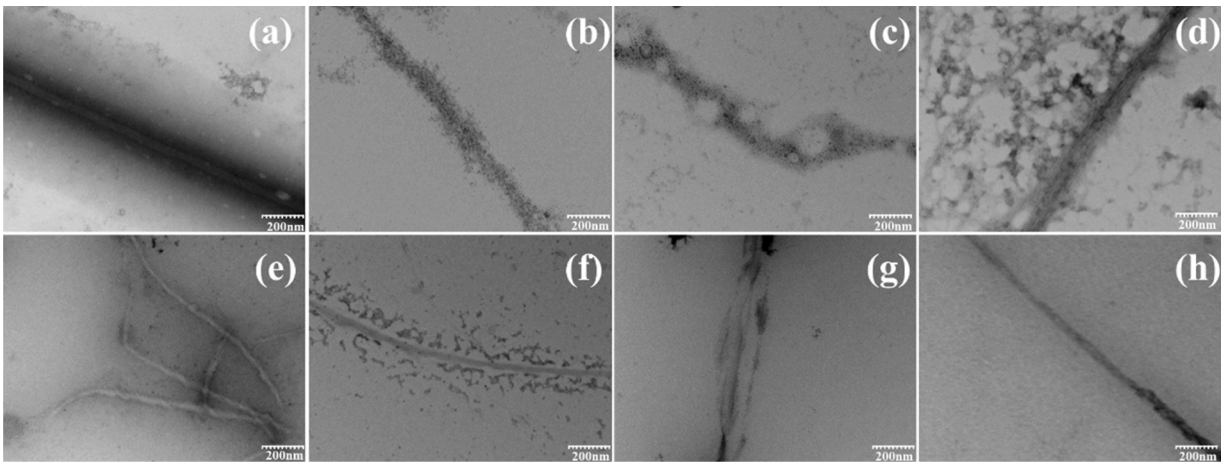

Fig. 5. TEM images (insert is the Ag element mapping) of CNF-DNA chelated with different concentrations of Ag^+ (0 (a), 1 (b), 10 (c), 20 (d), 40 (e), 60 (f), 80 (g), and 100 (h) nM).

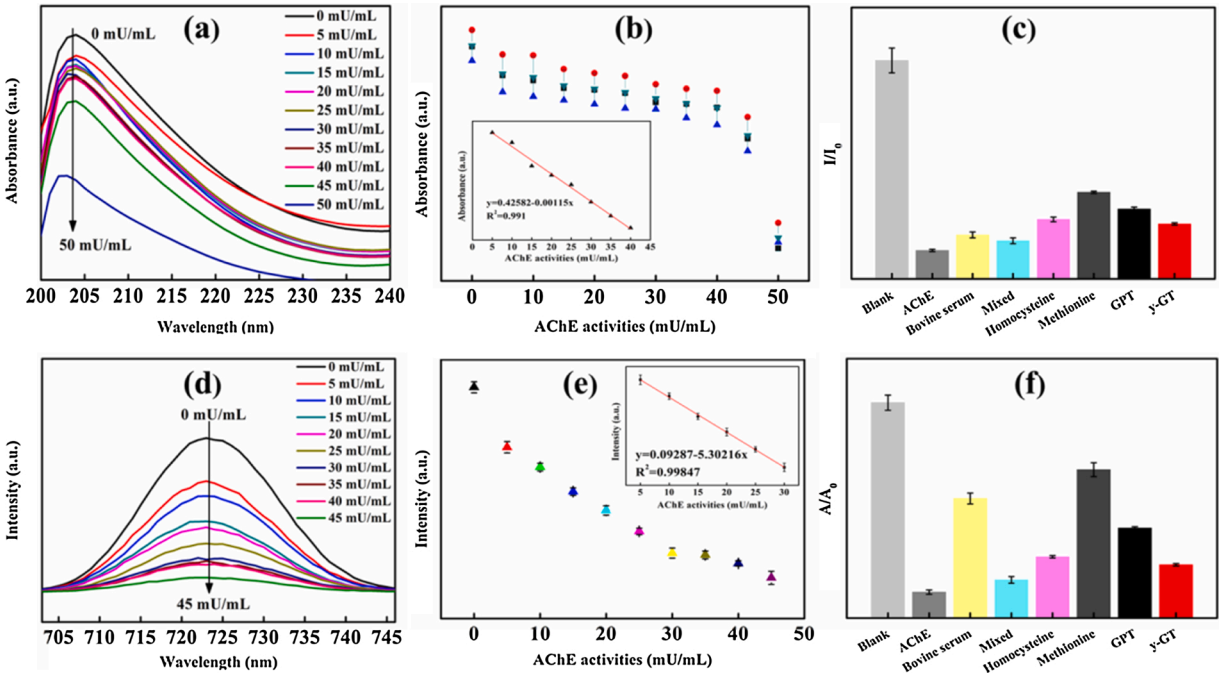

Fig. 6. UV–vis and fluorescence spectra: calibration curves (a, d) and standard curves (b, e) for the detection of different AChE activities by the CNF-DNA-AgNCs (0, 5, 10, 15, 20, 25, 30, 35, 40, and 45 mU/mL) and the selectivity (c, f) of the CNF-DNA-AgNCs towards the activity of AChE in the presence of other interference reagents.

by DNA on the surface of CNF-DNA. In addition, the ash residue mass of CNF-DNA increased by 5.98 wt% after the formation of the CNF-DNA-AgNCs (Fig. S8). The changes in the surface of CNF-DNA after the detection of Ag^+ are shown in Fig. S9. As can be observed from the figure, the surface of CNF-DNA became smoother after the chelation.

To investigate the Ag^+ recognition mechanism of CNF-DNA, geometry optimization was carried out using the extended tight binding program, the generalized born solvent-accessible implicit solvation model, and water as the solvent. As shown in Fig. 8, Ag^+ was surrounded by two phosphoric acid segments and two C groups. The shortest Ag—O (C) distance was 2.65 Å. The other C segment interacted with Ag^+ *via* both its N and O atoms to form Ag—N and Ag—O bonds with the bond lengths of 2.42 Å and 2.72 Å, respectively (Bannwarth et al., 2019; Grimme et al., 2017). Thus, only the Ag—O and Ag—N bond lengths met the requirement of the coordination bond distance (Movahedi et al., 2019; Kim et al., 2020; Zhang et al., 2018).

The Ag^+ selectivity of CNF-DNA was investigated by SEM, XPS, and density functional theory (DFT) analyses (Fig. 9). Theoretically, Ag^+ ions can interact with the cytosine base (C) to form a stable C-Ag^+-C mismatched complex (Ono et al., 2008; Wu et al., 2018; Kim et al., 2017). In fact, the grafted DNA have the apropos C on surface of CNF causing CNF-DNA more easy chelated with Ag^+ than other ions. The CNF-DNA-AgNCs showed Ag 3d peaks (366.08–382.08 eV) in the XPS survey spectra of CNF-DNA-AgNCs, the Ag 3d peak could be deconvoluted into a $3d_{5/2}$ peak at 368.68 eV and a $3d^{3/2}$ peak at 374.78 eV (Fig. 7**(b)**), associating spectra of O 1s and N 1s (Fig. 7**(c)**, **(d)**) and suggesting the —NH_2 and C═O groups of CNF-DNA preferentially chelated with Ag^+ and reduced it. Simultaneously, the interaction between Ag^+ and DNA caused conformational changes of DNA, inducing changes in the fluorescence of the DNA aptamer and signal. Based on the DFT simulation calculation of CNF-DNA after the detection of Ag^+, the C segment interacted with Ag^+ *via* both its N and O atoms to form Ag—N

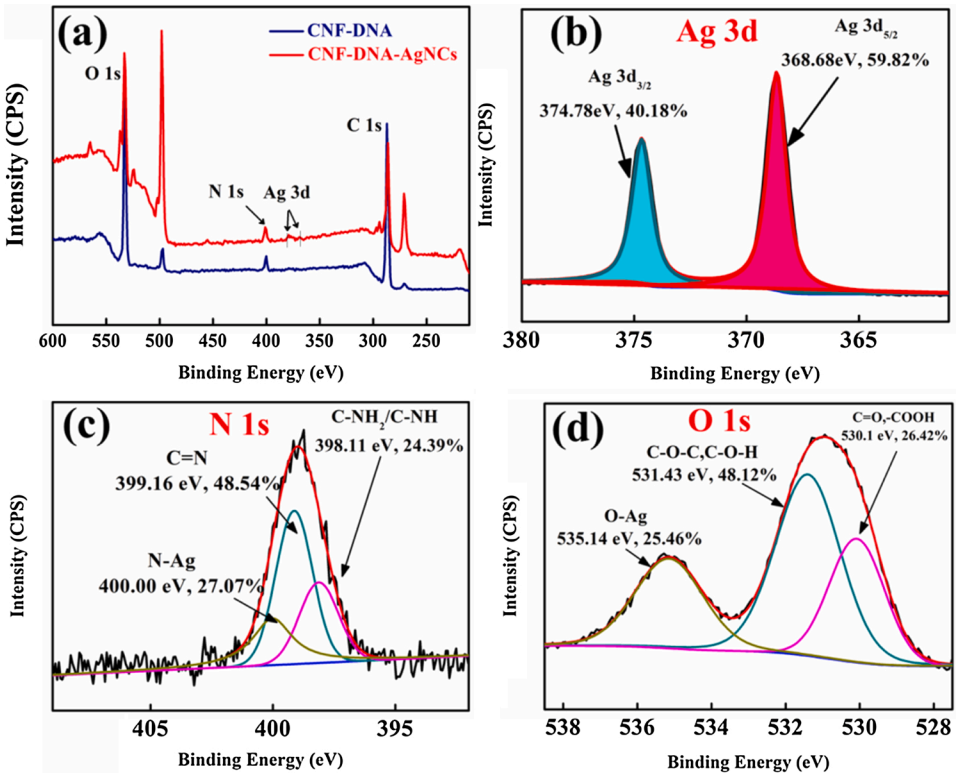

Fig. 7. XPS survey spectra of CNF-DNA and the CNF-DNA-AgNCs (a); the Ag 3d (b) N 1s (c) and O 1s spectra (d) of the CNF-DNA-AgNCs.

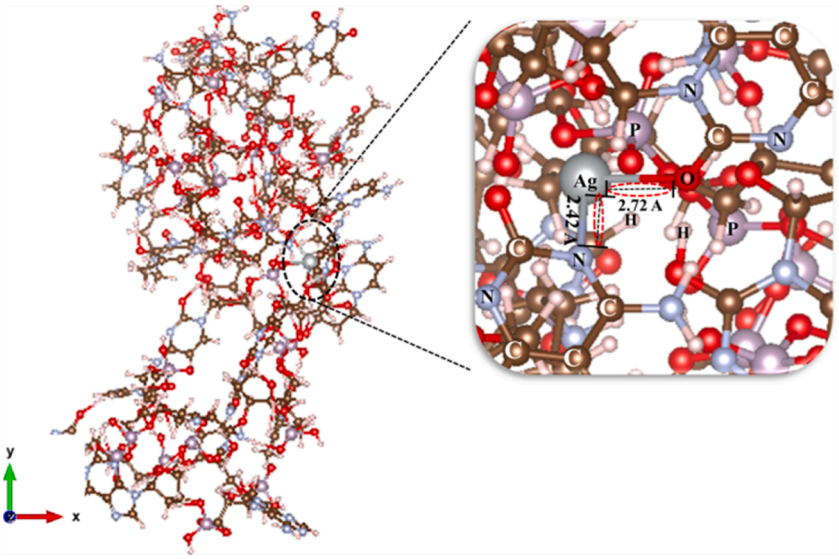

Fig. 8. DFT-optimized structure of CNF-DNA after the detection of Ag^{+}.

and Ag—O bonds with the bond lengths of 2.42 Å and 2.72 Å, respectively (Fig. 8). The bonding radii of Ag—N and Ag—O are both shorter than the sum of the metal ion radii of Ag^{+} (1.72 Å) (Liu et al., 2020) and the van der Waals radii of O (1.52 Å) or N (1.55 Å) (Kellou et al., 2006), thus meeting the requirement of the coordination bond distance (Soliman and Elsilk, 2018; Wen et al., 2020; Batsanov, 1999). The results indicated that the CNF-DNA possesses the high selectivity for Ag^{+}.

Thus, Ag^{+} was detected by CNF-DNA through chelation with its bidentate ligand (DNA). The amino and carbonyl groups of the cytosine bases in DNA formed N—Ag and O—Ag co-ordination bonds with Ag^{+}. Furthermore, the CNF-DNA-AgNCs could detect AChE. ATCh was used as the substrate for AChE. AChE caused the hydrolysis of ATCh to thiocholine. The sulfhydryl groups could react with the CNF-DNA-AgNCs, thus reducing their fluorescence.

3.6. *Biocompatibility of CNF-DNA*

The biocompatibility of CNF-DNA was evaluated by carrying out an *in vitro* cytotoxicity test (cell viability), an acute systemic toxicity test (clinical observation of the biological responses of animals), a skin sensitization test (sensitization-positive incidence), and a single-contact skin irritation test (primary stimulation index) (Fig. 10, Table S4). L929 cells were used to investigate the *in vitro* cytotoxicity of CNF-DNA. The viability of the cells treated with CNF-DNA was higher than 85 %

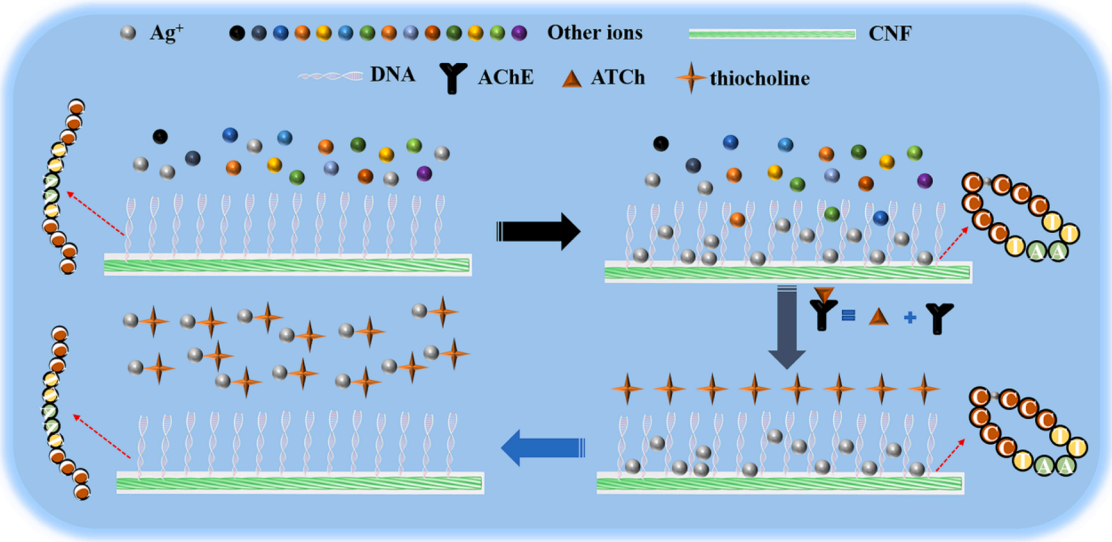

Fig. 9. Possible Ag^{+} and AChE recognition mechanisms of CNF-DNA.

(Fig. 10**(a)**), indicating that CNF-DNA showed no potential cytotoxicity. Male KM mice weighing 30–40 g were used as the experimental subjects for the acute systemic toxicity experiments. The weights of the CNF-DNA-exposed mice remained greater than 30 g for 72 h (Fig. 10**(b)**), and the biological response was no better than that of the vehicle control-treated animals, indicating that CNF-DNA was nontoxic. Furthermore, ordinary New Zealand rabbits (not pregnant and not produced) were used as the experimental animals for the single-contact skin irritation experiments (Fig. 10**(c)**). Unlike the positive control group, the rabbits exposed to CNF-DNA weighed more than 2.4 kg for 72 h after the exposure. The rabbits exposed to polar and nonpolar CNF-DNA showed no signs of erythema or edema, and the primary stimulation index was 0. Slight skin irritation was observed after the exposure to CNF-DNA. The skin sensitization tests were performed on normal-grade albino guinea pigs (Fig. 10**(d)**). The guinea pigs exposed to CNF-DNA weighed more than 30 g for 72 h after the treatment. None of the polar or nonpolar CNF-DNA treatments caused sensitization. In summary, the as-prepared CNF-DNA showed excellent biocompatibility, and hence huge potential for application in biosensors and biomarkers.

Fig. 11**(a)**–**(d)** show the strong green fluorescence of L929 cells after 24 h of incubation with CNF-DNA, indicating that all the cells were alive after the incubation (green fluorescence represented live cells). Fig. 11 **(e)**–**(h)** show the strong green fluorescence of the cellular membrane and the slight red fluorescence at 1000 μg/mL after 48 h of incubation, suggesting that only a few L929 cells were dead after the incubation with a high concentration of CNF-DNA for 48 h (red fluorescence represented dead cells).

4. Conclusions

A nanosized dual-function CNF-based bionic biosensor (CNF-DNA) was prepared by grafting a DNA aptamer onto the surface of CNFs, which were prepared from bagasse pulp cellulose fibers. The as-prepared CNF-DNA showed good biocompatibility and excellent selectivity and sensitivity for trace levels (1×10^{-6} nM) of Ag^{+} in the presence of other metal ions (Hg^{2+}, Ba^{2+}, Cd^{2+}, Mg^{2+}, Mn^{2+}, Pb^{2+}, and Zn^{2+}), as revealed by the UV–vis and fluorescence analyses. More importantly, the nanosized biomass-based bionic CNF-DNA could produce AgNCs (CNF-DNA-AgNCs) during the detection of Ag^{+}. The average size of the DNA-AgNCs formed on the surface of CNF-DNA

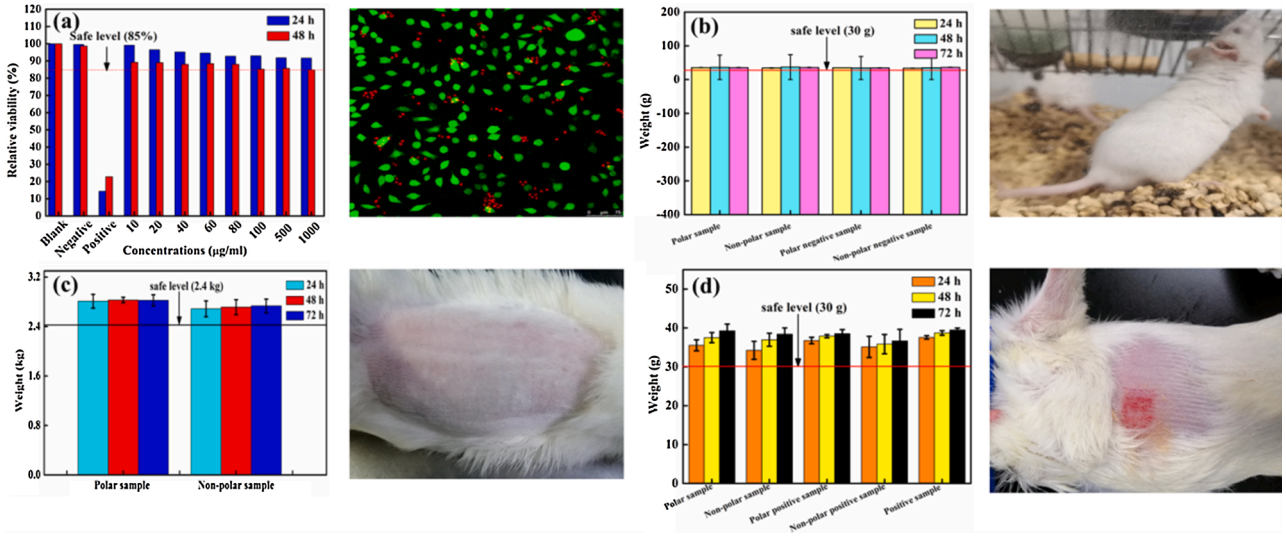

Fig. 10. Biocompatibility measurements: *in vitro* cytotoxicity (a), acute systemic toxicity (b), single contact skin irritation (c), and skin sensitization (d) tests of CNF-DNA.

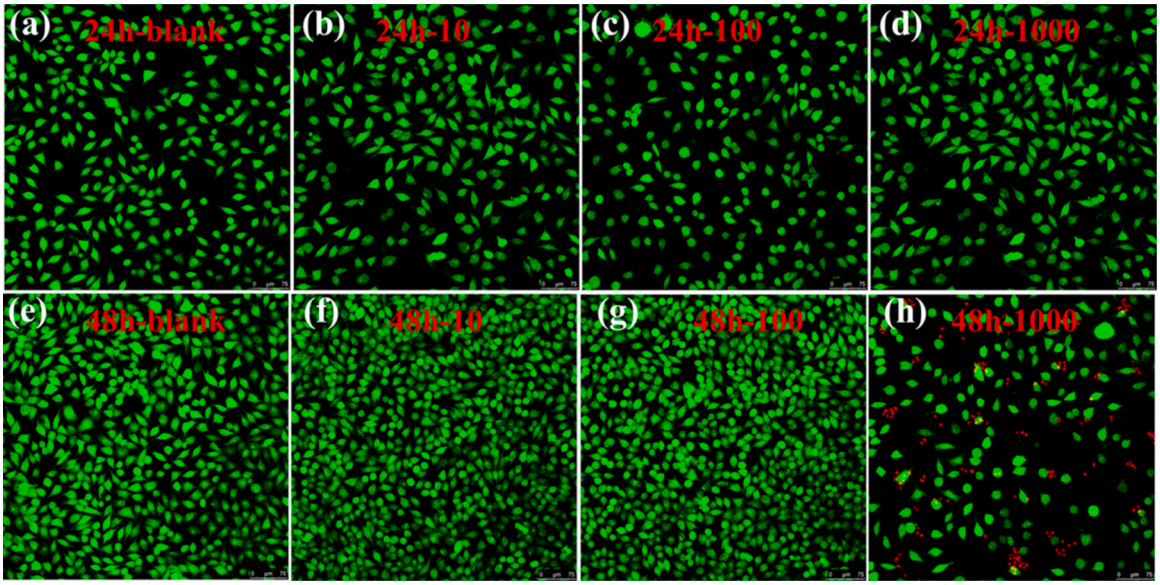

Fig. 11. LSCM images of L929 after the *in vitro* cytotoxicity test using CNF-DNA at different times and concentrations (24 h-blank (a), 24 h-10 (b), 24 h-100 (c), 24 h-1000 (d), 48 h-blank (e), 48 h-10 (f), 48 h-g (g) and 48 h-1000 (h)).

increased with an increase in the Ag^+ concentration. The smallest NC size was found to be 2.13 nm. These NCs could further detect AChE at the concentration of 0.053 mU/mL in the presence of bovine serum, homocysteine, methionine, GPT, and γ-GT. This chemical method of grafting DNA onto CNFs can overcome the instability and low signal limitations of DNA biosensors prepared by physical mixing. The CNF-DNA biosensor showed excellent selectivity and sensitivity for trace levels of Ag^+. The findings of this study will be useful for developing novel synthesis strategies for DNA-template AgNCs for AChE detection. This study will also be helpful for investigating novel structural templates that can be chemically anchored onto biomass NFs to prepare biomass-based bionic biosensors with multiple functions and potential for *in vivo* and *in vitro* detection for biomedical applications.

Ethics statement

All the biocompatibility tests were carried out with the assistance of Guangdong Neway Quality Technology Service Co., Ltd. in accordance with the relevant laws and institutional guidelines on the use of laboratory animals.

CRediT authorship contribution statement

Lei Wang: Conceptualization, Methodology, Software. **Wei Guo:** Data curation, Writing - original draft. **Hongxiang Zhu:** Visualization, Investigation. **Hui He:** Writing - review & editing. **Shuangfei Wang:** Supervision.

Declaration of Competing Interest

The authors declare that they have no known competing financial interests or personal relationships that could have appeared to influence the work reported in this paper.

Acknowledgments

All the authors thankfully acknowledge the financial support provided by the National Natural Science Foundation of China (31860193), the Guangxi Youth Natural Science Fund(2018GXNSFBA281174), the National Key R&D Program of China(2018YFD0800700), the Guangxi Science and Technology Research Program(14251009), and the Guangxi University Young Doctor Research Foundation Project (XBZ180057).

Appendix A. Supplementary data

Supplementary material related to this article can be found, in the online version, at doi:https://doi.org/10.1016/j.jhazmat.2020.123921.

References

Ahmed, M., Faisal, M., Ihsan, A., Naseer, M.M., 2019. Fluorescent organic nanoparticles (FONs) as convenient probes for metal ions detection in aqueous medium. Anal. (R. Soc. Chem.) 144, 2480–2497.
Al-Enizi, A.M., Ahamad, T., Al-hajji, A.B., Ahmed, J., Chaudhary, A.A., Alshehri, S.M., 2018. Cellulose gum and copper nanoparticles based hydrogel as antimicrobial agents against urinary tract infection (UTI) pathogens. Int. J. Biol. Macromol. 109, 803–809.
Bannwarth, C., Ehlert, S., Grimme, S., 2019. GFN2-xTB—an accurate and broadly parametrized self-consistent tight-binding quantum chemical method with multipole electrostatics and density-dependent dispersion contributions. J. Chem. Theory Comput. 15, 1652–1671.
Batsanov, S.S., 1999. Calculation of van der waals radii of atoms from bond distances. J. Mol. Struct.-theochem. 468, 151–159.
Burratti, L., Bolli, E., Casalboni, M., de Matteis, F., Mochi, F., Francini, R., Casciardi, S., Prosposito, P., 2019. Synthesis of fluorescent Ag nanoclusters for sensing and imaging applications. Mater. Sci. Forum 941, 2243–2248.
Camacho, A.S., Martín-García, I., Contreras-Celedón, C., Chacón-García, L., Alonso, F., 2017. DNA-supported palladium nanoparticles as a reusable catalyst for the copper- and ligand-free Sonogashira reaction. Catal. Sci. Technol. 7, 2262–2273.
Cho, S.-J., Kim, H.J., Hong, B., Boo, J.-H., 2011. A study on the plasma polymer thin film surface modification for DNA alignment by using high energy electron beam irradiation. Thin Solid Films 519, 7060–7064.
Choi, S., Lee, G., Park, I.S., Son, M., Kim, W., Lee, H., Lee, S.-Y., Na, S., Yoon, D.S., Bashir, R., Park, J., Lee, S.W., 2016. Detection of silver ions using dielectrophoretic tweezers-based force spectroscopy. Anal. Chem. 88, 10867–10875.
Desai, M.L., Basu, H., Singhal, R.K., Saha, S., Kailasa, S.K., 2019. Ultra-small two dimensional MXene nanosheets for selective and sensitive fluorescence detection of Ag^+ and Mn^{2+} ions. Colloids Surf. A: Physicochem. Eng. Asoects 565, 70–77.
Ganapathy, S., Naito, A., McDowell, C., 1981. Paramagnetic doping as an aid in obtaining high-resolution ^{13}C NMR spectra of biomolecules in the solid state. J. Am. Chem. Soc. 103, 6011–6015.
Gao, R., Xu, G., Zheng, L., Xie, Y., Tao, M., Zhang, W., 2016. A highly selective and sensitive reusable colorimetric sensor for Ag^+ based on thiadiazole-functionalized polyacrylonitrile fiber. J. Mater. Chem. C 4, 5996–6006.
Goh, H., Nam, T.K., Singh, A., Singh, N., Jang, D.O., 2017. Dipodal colorimetric sensor for Ag^+ and its resultant complex for iodide sensing using a cation displacement approach in water. Tetrahedron Lett. 58, 1040–1045.
Grimme, S., Bannwarth, C., Shushkov, P., 2017. A robust and accurate tight-binding quantum chemical method for structures, vibrational frequencies, and noncovalent

interactions of large molecular systems parametrized for all spd-block elements (Z = 1–86). J. Chem. Theory Comput. 13, 1989–2009.
Guo, Z., Zheng, Y., Xu, H., Zheng, B., Qiu, W., Liu, G., 2017. Lateral flow test for visual detection of silver(I) based on cytosine-Ag(I)-cytosine interaction in C-rich oligonucleotides. Microchim. Acta 184, 4243–4250.
Guo, W., He, H., Zhu, H., Hou, X., Lin, J., 2019. Preparation and properties of a biomass cellulose-based colorimetric sensor for Ag^{+} and Cu^{2+}. Ind. Crops Prod. 137, 410–418.
Han, S., Park, J., Byun, M.S., Yi, D., Lee, J.H., Lee, D.Y., Mookjung, I., 2019. Blood acetylcholinesterase level is a potential biomarker for the early detection of cerebral amyloid deposition in cognitively normal individuals. Neurobiol. Aging 73, 21–29.
He, L., Yang, L., Zhu, H., Dong, W., Ding, Y., Zhu, J.-J., 2017. A highly sensitive biosensing platform based on upconversion nanoparticles and graphene quantum dots for the detection of Ag+. Method. Appl. Fluoresc. 5, 024010.
He, H., Cheng, M., Liang, Y., Zhu, H., Sun, Y., Dong, D., Wang, S., 2020. Intelligent cellulose nanofibers with excellent biocompatibility enable sustained antibacterial and drug release via a pH-responsive mechanism. J. Agric. Food. Chem. 68, 3518–3527.
Jiang, X., Xu, W., Chen, X., Liang, Y., 2019. Colorimetric assay of Hg^{2+} based on the inhibition of peroxidase mimetic activity of gold nanoclusters induced by Hg^{2+}. Anal. Methods 11, 2179–2182.
Katuli, K.K., Massarsky, A., Hadadi, A., Pourmehran, Z., 2014. Silver nanoparticles inhibit the gill Na^{+}/K^{+}-ATPase and erythrocyte AChE activities and induce the stress response in adult zebrafish (Danio rerio). Ecotoxicol. Environ. Safety 106, 173–180.
Kellou, A., Grosdidier, T., Aourag, H., 2006. Comparative behavior of vacancy and C, B, N, O atoms single defect on hardening the B_2-FeAl structure: an atomistic study. Intermetallics 14, 142–148.
Khoris, I.M., Takemura, K., Lee, J., Hara, T., Abe, F., Suzuki, T., Park, E.Y., 2019. Enhanced colorimetric detection of norovirus using in-situ growth of Ag shell on Au NPs. Biosens. Bioelectron. 126, 425–432.
Kim, J.H., Kim, K.B., Park, J.S., Min, N., 2017. Single cytosine-based electrochemical biosensor for low-cost detection of silver ions. Sens. Actuators B 245, 741–746.
Kim, S., Lee, H., Chae, J.B., Kim, C., 2020. A pyrene-mercapto-based probe for detecting Ag^{+} by fluorescence turn-on. Inorg. Chem. Commun. 118, 108044.
Ko, H.E., Kwan, S.G., Park, H.W., Caron, A., 2017. Chemical effects on the sliding friction of Ag and Au(111). Friction 6, 1–14.
Kosmidis, M.H., Vlachos, G.S., Anastasiou, C.A., Yannakoulia, M., Dardiotis, E., Hadjigeorgiou, G., Sakka, P., Ntanasi, E., Scarmeas, N., 2018. Dementia prevalence in Greece: the hellenic longitudinal investigation of aging and diet (HELIAD). Alzheimer Dis. Assoc. Disord. 32, 232–239.
Kruer-Zerhusen, N., Cantero-Tubilla, B., Wilson, D.B., 2017. Characterization of cellulose crystallinity after enzymatic treatment using Fourier transform infrared spectroscopy (FTIR). Cellulose 25, 1–12.
Li, W.-T., Wu, G.-Y., Qu, W.-J., Li, Q., Lou, J.-C., Lin, Q., Yao, H., Zhang, Y.-M., Wei, T.-B., 2017. A colorimetric and reversible fluorescent chemosensor for Ag^{+} in aqueous solution and its application in IMPLICATION logic gate. Sens. Actuators B: Chem. 239, 671–678.
Liu, G., Yuan, Y., Wang, J., 2016. Hemin/G-quadruplex DNAzyme nanowires amplified luminol electrochemiluminescence system and its application in sensing silver ions. RSC Adv. 6, 37221–37225.
Liu, J.-J., Yu, L.-M., Han, F.-X., Chen, F.-Y., Cheng, F.-X., 2019. A thioether-containing luminescent metal-organic framework for highly selective and sensitive detection of Ag(I) ion. J. Solid State Chem. 270, 45–50.
Liu, W.-E., Chen, Z., Yang, L.-P., Au-Yeung, H.Y., Jiang, W., 2019. Molecular recognition of organophosphorus compounds in water and inhibition of their toxicity to acetylcholinesterase. Chem. Commun. 55, 9797–9800.
Liu, W.-E., Chen, Z., Yang, L.-P., Au-Yeung, H.Y., Jiang, W., 2019. Molecular recognition of organophosphorus compounds in water and inhibition of their toxicity to acetylcholinesterase. Chem. Commun. 55, 9797–9800.
Liu, J., Wang, S., Li, W., Dong, Y., Wang, J., Song, Q., Zhang, C., 2020. A novel imidazole-based tri-nitrogen metal cations probe with better-selectivity in ionic radius and acting as a Zn^{2+} fluorescence turn-on sensor. J. Mol. Struct. 1222, 128909.
Long, Q., Wen, Y., Li, H., Zhang, Y., Yao, S., 2017. A novel fluorescent biosensor for detection of silver ions based on upconversion nanoparticles. J. Fluorescence 27, 205–211.
Mansour, R.S.H., Sallam, A.A., Hamdan, I.I., Khalil, E.A., Yousef, I., 2017. Elucidation of penetration enhancement mechanism of emu oil using FTIR microspectroscopy at EMIRA laboratory of SESAME synchrotron. Spectrochim. Acta Part A: Mol. Biomol. Spec. 185, 1–10.
Minnes, R., Nissinmann, M., Maizels, Y., Gerlitz, G., Raichlin, Y., 2017. Using attenuated total reflection–fourier transform Infra-Red (ATR-FTIR) spectroscopy to distinguish between melanoma cells with a different metastatic potential. Sci. Rep. 7, 4381.
Movahedi, E., Rezvani, A.R., Razmazma, H., 2019. Binding interaction of a heteroleptic silver(I) complex with DNA: a joint experimental and computational study. Int. J. Biol. Macromol. 126, 1244–1254.
Ono, A., Cao, S., Togashi, H., Tashiro, M., Fujimoto, T., Machinami, T., Oda, S., Miyake, Y., Okamoto, I., Tanaka, Y., 2008. Specific interactions between silver(i) ions and cytosine–cytosine pairs in DNA duplexes. Chem. Commun. 4825–4827.
Pargar, F., Kolev, H., Koleva, D.A., Breugel, K.V., 2018. Microstructure, surface chemistry and electrochemical response of Ag|AgCl sensors in alkaline media. J. Mater. Sci. 53, 7527–7550.
Rieger, K.A., Cho, H.J., Yeung, H.F., Fan, W., Schiffman, J.D., 2016. Antimicrobial activity of silver ions released from zeolites immobilized on cellulose nanofiber mats. ACS Appl. Mater. Interfaces 8, 3032–3040.
Rivilla, I., Aparicio, B., Bueno, J.M., Casanova, D., Tonnelé, C., Freixa, Z., Herrero, P., Rogero, C., Miranda, J.I., Martínez-Ojeda, R.M., Monrabal, F., Olave, B., Schäfer, T., Artal, P., Nygren, D., Cossío, F.P., Gómez-Cadenas, J.J., 2020. Fluorescent bicolour sensor for low-background neutrinoless double β decay experiments. Nature 583, 48–54.
Soliman, S.M., Elsilk, S.E., 2018. Synthesis, X-ray structure, DFT and antimicrobial studies of Ag(I) complexes with nicotinic acid derivatives. J. Photochem. Photobiol. B: Biol. 187, 48–53.
Spacciapoli, P., Buxton, D., Rothstein, D., Friden, P., 2001. Antimicrobial activity of silver nitrate against periodontal pathogens. J. Periodontal Res. 36, 108–113.
Sun, J., Gan, Y., Liang, T., Zhou, S., Wang, X., Wan, H., Wang, P., 2019. Signal enhancement of electrochemical DNA biosensors for the detection of trace heavy metals. Curr. Opin. Electrochem. 17, 23–29.
Tian, D., Li, T., Zhang, R., Wu, Q., Chen, T., Sun, P., Ramamoorthy, A., 2017. Conformations and intermolecular interactions in Cellulose/Silk fibroin blend films: a solid-State NMR perspective. J. Phys. Chem. B 121, 6108–6116.
Volkov, I.L., Smirnova, A., Makarova, A.A., Reveguk, Z.V., Ramazanov, R.R., Usachov, D. Y., Adamchuk, V.K., Kononov, A.I., 2017. DNA with ionic, atomic, and clustered silver: an XPS study. J. Phys. Chem. B 121, 2400–2406.
Wang, F., Lu, Y., Chen, Y., Sun, J., Liu, Y., 2018. Colorimetric nanosensor based on the aggregation of AuNP triggered by carbon quantum dots for detection of Ag^{+} ions. ACS Sustain. Chem. Eng. 6, 3706–3713.
Wang, G., Shao, C., Yan, C., Li, D., Liu, Y., 2019. Fluorescence polarization sensor platform based on gold nanoparticles for the efficient detection of Ag (I). J. Lumin. 210, 21–27.
Wang, M., Liu, L., Xie, X., Zhou, X., Lin, Z., Su, X., 2020. Single-atom iron containing nanozyme with peroxidase-like activity and copper nanoclusters based ratio fluorescent strategy for acetylcholinesterase activity sensing. Sens. Actuators B: Chem. 313, 128023.
Wen, L., Ren, C., Zou, Y., Lin, W., Ding, K., 2020. Why it is S-rich around Mo atom in the nitrogenase: a DFT investigation. Appl. Surf. Sci. 534, 147595.
Wolfe, M.G., Ali, M.M., Brennan, J.D., 2019. Enzymatic litmus test for selective colorimetric detection of C–C single nucleotide polymorphisms. Anal. Chem. 91, 4735–4740.
Wu, Y., Jiang, T., Wu, Z., Yu, R., 2018. Internal standard-based SERS aptasensor for ultrasensitive quantitative detection of Ag+ ion. Talanta 185, 30–36.
Xing, X., Yang, H., Tao, M., Zhang, W., 2015. An overwhelmingly selective colorimetric sensor for Ag^{+} using a simple modified polyacrylonitrile fiber. J. Hazard. Mater. 297, 207–216.
Xu, Y., Zhang, C., Du, H., Li, Q., Zhang, H., Luo, X., 2019. Fluorometric detection of silver (I) using cytosine-Ag(I)-cytosine pair formation, DNA assembly and the AND logic operation of a multiple-component DNAzyme. Microchim. Acta 186, 522.
Xu, S., Chen, X., Chen, X., Liang, Y., 2019. Methylene blue-based distinguishing DNA conformation for colorimetric detection of silver ions. Microchem. J. 147, 995–998.
Zhang, B., Wei, C., 2017. A label-free fluorescent sensor based on structure-switching oligonucleotides for the detection of Ag^{+}, biothiols and acetylcholinesterase activity. ChemistrySelect 2, 6844–6849.
Zhang, P., Niu, Y., Qiao, W., Xue, Z., Bai, L., Chen, H., 2018. Experimental and DFT investigation on the adsorption mechanism of silica gel supported sulfur-capped PAMAM dendrimers for Ag(I). J. Mol. Liq. 263, 390–398.
Zhao, Y., Zhou, H., Zhang, S., Xu, J., 2019. The synthesis of metal nanoclusters and their applications in bio-sensing and imaging. Method. Appl. Fluoresc. 8, 012001.
Zhou, H., Zhu, H., Xue, F., He, H., Wang, S., 2020. Cellulose-based amphoteric adsorbent for the complete removal of low-level heavy metal ions via a specialization and cooperation mechanism. Chem. Eng. J. 385, 123879.
Zhu, C., Soldatov, A., Mathew, A.P., 2017. Advanced microscopy and spectroscopy reveal the adsorption and clustering of Cu (II) onto TEMPO-oxidized cellulose nanofibers. Nanoscale 9, 7419–7428.
Zhu, H., Guo, W., Wang, J., He, H., Hou, X., Zhou, S., Wang, S., 2019. Tuneable design of a pulp fibre-based colorimetric sensor and its visual recognition mechanism for ppb levels of Ag+. Cellulose 26, 9149–9161.
Zuo, X., Zhang, H., Zhu, Q., Wang, W., Feng, J., Chen, X., 2016. A dual-color fluorescent biosensing platform based on WS2 nanosheet for detection of Hg^{2+} and Ag^{+}. Biosens. Bioelectron. 85, 464–470.